ANEJO 04:

MEDIO FÍSICO

ÍNDICE

ÍNDICE ILUSTRACIONES

ÍNDICE TABLAS

1 OBJETO

En el siguiente Anejo se realizará un estudio de todo el medio físico necesario para realizar el diseño del proyecto básico del puerto de El Perelló.

En primer lugar, se realizará una caracterización del oleaje para regímenes medios. No se realizará una caracterización del oleaje para regímenes extremales debido a que no se realizará ninguna actuación sobre las obras de abrigo y, tal solo, necesitaremos las condiciones de operatividad durante un año medio. Además, se realizará una propagación del oleaje desde aguas profundas hasta el interior de nuestra dársena deportivo.

En segundo lugar, se realizará una caracterización del viento tanto para regímenes extremales como en regímenes normales.

Por último, se realizará un estudio del nivel del agua que alcanza a lo largo del año.

2 CARACTERIZACIÓN DEL OLEAJE

2.1 DATOS DE PARTIDA

Para realizar la caracterización del oleaje se han empleado los datos actualizados del Banco de Datos Oceanográficos de Puertos del Estado del Ente Público Puertos del Estado, concretamente a los registros de la boya de Valencia, código 2630.

Ilustración 4.1. Boyas del Banco de Datos Oceanográficos de Puertos del Estado

El conjunto de datos de la Red Exterior está formado por las medidas procedentes de la Red de Boyas de Aguas Profundas de Puertos del Estado. Las boyas de esta red se caracterizan por estar fondeados lejos de la línea de costa a gran profundidad. Por lo tanto, las medidas de oleaje de estos sensores no están perturbadas por efectos locales.

Concretamente, la boya de Valencia (código 2630) se encuentra fondeada a una profundidad de 260 metros, en las coordenadas geográficas definidas por su latitud y longitud (Latitud = 39,52° N, Longitud = 0,21° E), desde septiembre del 2005 hasta la actualidad.

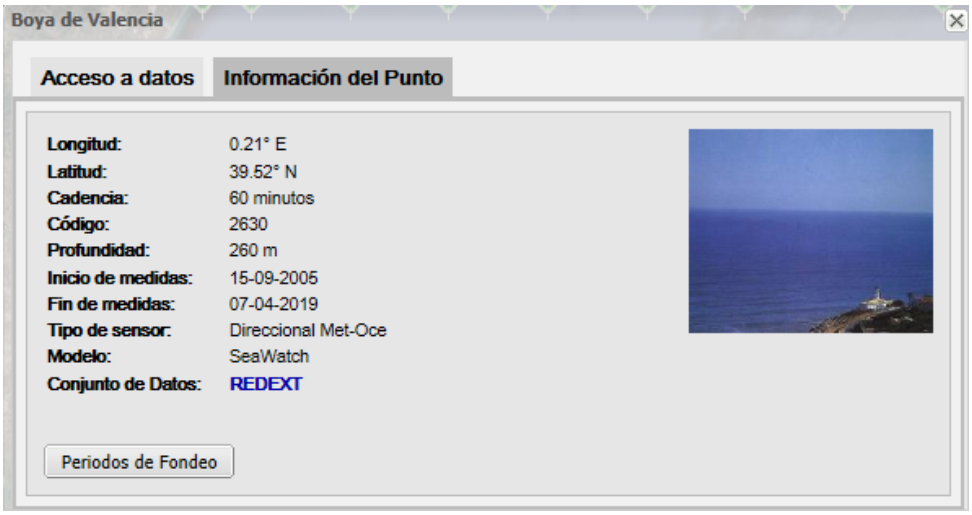

Ilustración 4.2. Información Boya de Valencia, código 2630.

Para asegurarnos de que los datos que nos proporciona la Boya de Valencia están realmente en aguas profundas y que los datos no se ven afectados por el fondo marino, se realiza una comprobación de profundidades.

En el caso de que nos encontremos en aguas profundas, se debe cumplir la siguiente relación:

$$\frac{d}{L_0} \geq 0{,}5 \quad \left(siendo\ L_0 = \frac{T_p^2 \cdot g}{2 \cdot \pi} \right)$$

Para obtener el periodo pico, utilizamos los datos referidos al régimen extremal para un periodo de retorno de T= 475 metros.

- H_s : $8{,}76\ m$
- T_p : $3.48 \cdot H_s^{0.63} = 3.48 \cdot 8.76^{0.63} = 13{,}657\ seg$

Donde, la longitud de la onda para este periodo es de:

$$L_0 : \frac{T_p^2 \cdot g}{2 \cdot \pi} = 261{,}2\ metros$$

$$d_0 : \frac{L_0}{2} = 130.6\ m < 260\ m$$

$$\frac{d}{L_0} = \frac{260}{261{,}2} = 0.9954 > 0.5$$

Con estas comprobaciones podemos establecer que los datos pertenecientes de la boya se encuentran en aguas profundas, por lo que podemos realizar la suposición de que son la representación del oleaje incidente en nuestra zona de estudio.

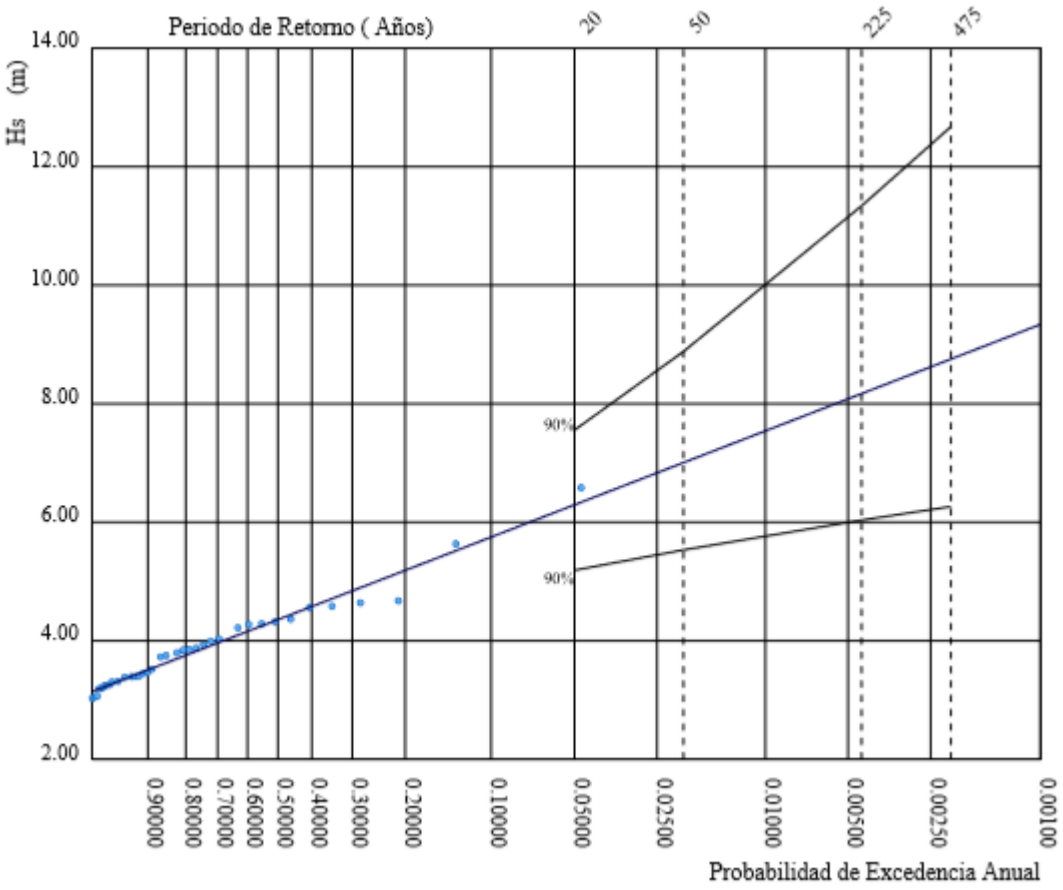

Ilustración 4.3. Régimen extremal escalar de oleaje. Boya de Valencia

2.2 CARACTERIZACIÓN DEL OLEAJE REGÍMENES MEDIOS

Se puede definir como régimen medio de una serie temporal al conjunto de estados de oleaje que más probablemente nos podemos encontrar. Dicho de otra forma, el régimen medio relaciona los diversos valores de la variable altura de ola significante con la probabilidad de que los valores no sean superados en el año climático medio.

La distribución de Wiebull que describe el régimen medio de las series de oleaje es la siguiente:

$$F_e(x) = 1 - \exp\left(-\left(\frac{x-B}{A}\right)^C\right)$$

Una de las principales utilidades de realizar una caracterización del régimen medio reside en las condiciones medias de operatividad. Es decir, a partir del régimen medio es posible caracterizar el comportamiento probabilístico del régimen de oleaje en el que por término medio se va a desarrollar una determinada actividad.

Según el *Atlas de Clima Marítimo* publicado en la *ROM 0.3-91: Oleaje*, la zona de estudio pertenece al Área VII y las direcciones significantes, para la zona de Valencia, abarcan del NE al SE, según se indica en la siguiente ilustración:

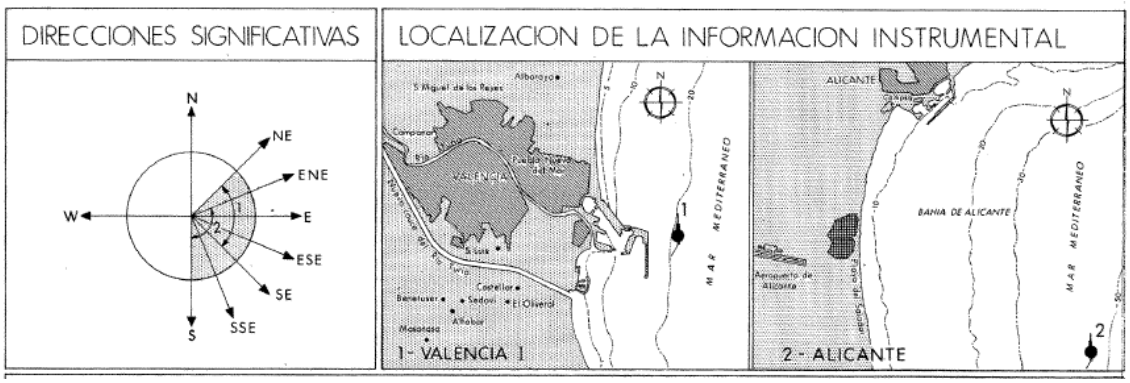

Ilustración 4.4. Atlas de Clima Marítimo, Área VII. ROM 0.3-91

En nuestra zona de estudio, según refleja los datos de la boya de Valencia, se tiene, por un lado, la distribución conjunta anual de periodo pico y altura de ola significativa, donde se relacionan la probabilidad de ocurrencia de una cierta altura de ola significante para un cierto periodo pico *(tabla 4.1)*. En la *tabla 4.2*, se muestra la media ponderada del periodo pico asociado a cada altura de ola significante. También se relaciona, en la *tabla 4.3,* la probabilidad de ocurrencia de una altura de ola significante en función de una dirección de propagación.

Tabla 4.1. Probabilidad de ocurrencia altura de ola significante (Hs) con periodo pico (Tp)

Hs (m)	Tp (s)											TOTAL
	1	2	3	4	5	6	7	8	9	10	11	
≤ 0.5		0.041	4.099	9.038	8.34	6.957	3.66	0.937	0.159	0.149	0.007	33.387
1			1.075	12.38	12.004	6.816	5.423	4.144	0.646	0.149	0.01	42.647
1.5				0.774	6.971	2.689	1.752	2.094	1.123	0.484	0.003	15.89
2					0.964	1.445	0.788	0.774	0.463	0.584	0.038	5.056
2.5					0.014	0.263	0.415	0.38	0.207	0.339	0.045	1.663
3						0.031	0.131	0.18	0.121	0.145	0.038	0.646
3.5						0.003	0.052	0.138	0.069	0.111	0.021	0.394
4							0.003	0.076	0.041	0.055	0.017	0.192
4.5								0.007	0.014	0.031	0.01	0.062
5								0.003	0.007	0.007	0.007	0.024
>5									0.003	0.021	0.015	0.039
TOTAL	0	0.041	5.174	22.192	28.293	18.204	12.224	8.733	2.853	2.075	0.211	100

Tabla 4.2. Media ponderada periodo pico para cada altura de ola significante

Hs (m)	Tp (s)
≤ 0.5	5.035
1	5.444
1.5	6.172
2	7.046
2.5	8.022
3	8.514
3.5	8.751
4	9.036
4.5	9.710

Hs (m)	Tp (s)
5	9.750
>5	10.308

Tabla 4.3. Probabilidad de ocurrencia direccional de la altura de ola significante

DIRECCIÓN		Hs (m)												TOTAL
		≤ 0.2	0.5	1	1.5	2	2.5	3	3.5	4	4.5	5	>5	
CALMAS		3.794												3.794
N	0		0.279	0.6	0.414	0.207	0.062	0.021	0.003					1.586
NNE	22.5		0.752	1.883	1.321	0.586	0.135	0.062	0.017	0.003	0.003			4.762
NE	45		1.921	4.933	2.677	1.09	0.514	0.224	0.155	0.086	0.024	0.01	0.028	11.662
ENE	67.5		4.005	7.34	3.353	1.445	0.697	0.276	0.183	0.093	0.034	0.014	0.01	17.45
E	90		4.967	5.012	1.09	0.348	0.103	0.028	0.017	0.007				11.572
ESE	112.5		4.898	3.439	0.448	0.1	0.017	0.014	0.003	0.003				8.922
SE	135		5.595	4.405	0.269	0.041	0.007							10.317
SSE	157.5		3.732	5.64	1.228	0.124	0.003							10.727
S	180		1.104	1.211	0.172	0.021								2.508
SSW	202.5		0.717	1.093	0.155	0.031								1.996
SW	225		0.842	2.88	0.931	0.059								4.712
WSW	247.5		0.4	2.525	2.408	0.566	0.059	0.007	0.003					5.968
WSW	270		0.128	0.566	0.548	0.124	0.034	0.007						1.407
WNW	292.5		0.135	0.335	0.314	0.11	0.007							0.901
NW	315		0.093	0.352	0.321	0.086	0.014							0.866
NNW	337.5		0.155	0.348	0.21	0.107	0.007	0.003	0.02					0.85
TOTAL		3.794	29.723	42.562	15.859	5.045	1.659	0.642	0.401	0.192	0.061	0.024	0.038	100

Centrándonos en nuestras direcciones de estudio, tenemos la siguiente media ponderada de las alturas de ola en función de la dirección de propagación:

Tabla 4.4. Alturas de ola (m) direcciones principales

Dirección	Hs (m)
NE	1.308
ENE	1.211
E	0.886
ESE	0.770
SE	0.747

Debido a que tenemos que garantizar la operatividad mínima dentro de la dársena del puerto, se debe calcular la altura de ola con un valor umbral cuya probabilidad de no excedencia no sea inferior al de un determinado valor. Para fijar dicha probabilidad, se parte del Índice de Repercusión Económica Operativa, IREO, calculado en el *Anejo 03: Carácter General y Operativo de las obras:*

Tabla 4.5. Índice de Repercusión Económica Operativa

IREO	$R_{f,ELO}$
4	**0.85**

Siendo $R_{f,ELO}$ el índice de fiabilidad, es decir, la operatividad mínima del tramo de obra frente a todos los modos principales adscritos a los estados límite de parada en su vida útil. Es por ello por lo que se fija una probabilidad de no excedencia de 0.85. Por lo tanto, se va a ajustar la altura de ola significante con los diferentes parámetros de la distribución de *Wiebull* para cada dirección de estudio diferente:

Tabla 4.6. Ajuste de la altura de ola significante

Dirección	NE	ENE	E	ESE	SE
F(Ha)	0.85	0.85	0.85	0.85	0.85
A	1.08	1.07	0.45	0.29	0.28
B	0	0	0.19	0.22	0.23
C	1.81	1.68	1.05	0.95	1.12
Hs,boya	1.54	1.57	1.02	0.79	0.73

Y, para cada altura de ola significante se le asocia su correspondiente periodo pico:

Tabla 4.7. Periodo pico (seg) para cada altura de ola direccional

Dirección	Hs,boya	Tp,boya
NE	1.54	6.24
ENE	1.57	6.29
E	1.02	5.47
ESE	0.79	5.27
SE	0.73	5.22

2.2.1 Propagación del oleaje

En el siguiente punto se realizará la propagación del oleaje desde los datos obtenidos en la boya, en aguas profundas, hasta las proximidades de la costa, en aguas reducidas. A medida que el oleaje se va acercando a la costa, sufre diversas modificaciones y amortiguamientos debidos al fondo marino, asomeramiento y refracción, y la presencia de obstáculos, difracción, que provoca una disminución de la altura de ola significante.

En primera medida, al disminuir la profundidad, cuando nos encontramos en situaciones de $d/L < 0.5$ y nos encontramos en zona de aguas intermedias, aparece un cambio de altura de ola debido a cambios en la celeridad de grupo C_0, la longitud de la ola disminuye y se aumenta el peralte de ésta. Este fenómeno se denomina **asomeramiento**, como se puede ver en la siguiente ilustración**.**

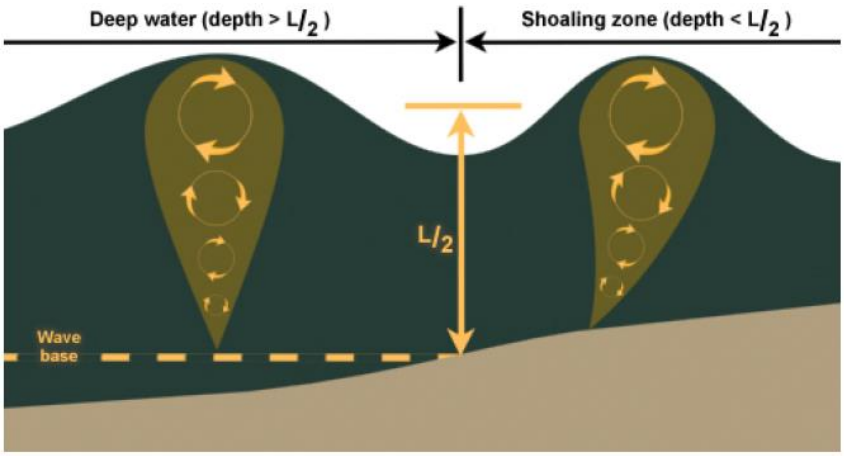

Ilustración 4.5. Fenómeno de asomeramiento

Y se representa analíticamente mediante la siguiente expresión:

$$\frac{H}{H_0} = \sqrt{\frac{1}{2} \cdot \frac{1}{n} \cdot \frac{C_0}{C}} = \sqrt{\frac{1}{2} \cdot \frac{1}{n} \cdot \frac{1}{\tanh\left(\frac{2 \cdot \pi \cdot d}{L}\right)}} = \sqrt{\frac{1}{\tanh\left(\frac{2 \cdot \pi \cdot d}{L}\right)} \cdot \frac{1}{\left[1 + \frac{4 \cdot \pi \cdot \frac{d}{L}}{senh\left(4 \cdot \pi \cdot \frac{d}{L}\right)}\right]}} = K_s$$

Donde K_s se define como el *coeficiente de asomeramiento*.

Por otro lado, a medida que el frente de onda se acerca a la costa, tiende a ponerse perpendicular a ella. Esto es debido al fenómeno de la **refracción**, dónde para un mismo frente de onda tenemos diferentes celeridades de onda, más lenta cuanta menos profundidad tengamos y viceversa, como se puede observar en la siguiente ilustración.

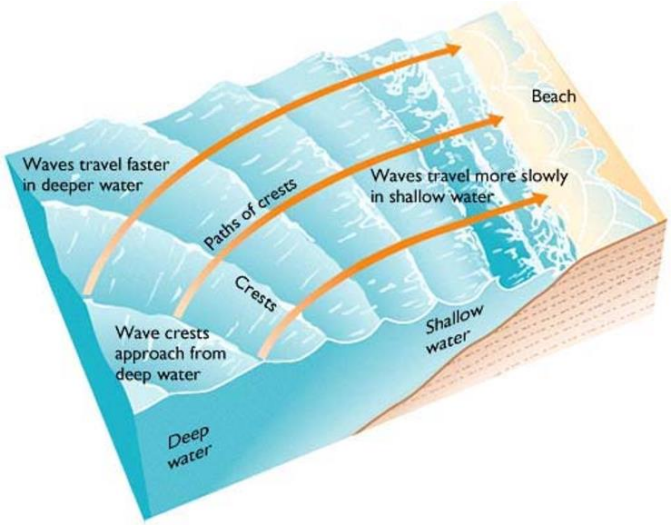

Ilustración 4.6. Fenómeno de refracción

En este caso, se denomina *coeficiente de refracción* a K_r y se representa mediante la siguiente expresión analítica:

$$K_r = \sqrt{\frac{b_0}{b1_1}} = \sqrt{\frac{\cos\alpha_0}{\cos\alpha_1}}$$

Por lo tanto, para la propagación del oleaje desde la boya hasta las proximidades del puerto se debe multiplicar ambos coeficientes por la altura de ola significante de la boya:

$$H_s = H_{s,0} \cdot K_s \cdot K_r$$

Como se pudo observar en el *Anejo 02. Topografía y Batimetría*, el perfil del fondo marino es prácticamente paralelo a la línea de costa y presenta una inclinación respecto al norte de, aproximadamente, 65°. Además, la obra de abrigo del puerto de El Perelló se encuentra a una profundidad de 3 metros.

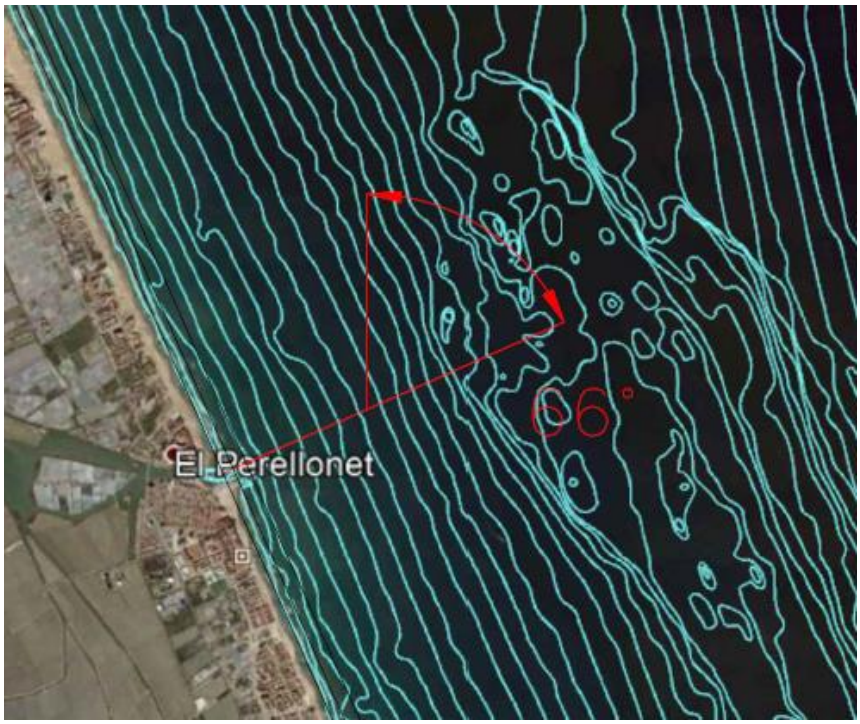

Ilustración 4.7. Orientación de la línea de costa

En las siguientes tablas se reflejará la propagación del oleaje desde una profundidad de 200 m hasta encontrarnos con nuestra obra de abrigo para las direcciones de propagación que presentan una mayor altura de ola, en nuestro caso, NE y ENE, y para la dirección SE, que como pudimos observar en el *Anejo 01: Antecedente y estado actual*, es la dirección que provocaba una gran agitación dentro de la dársena deportiva del puerto de El Perelló:

Tabla 4.8. Propagación del oleaje para NE (20°N)

d	d/Lo	th(2πd/L)	d/L	L	C	Cg	α	Ks	Kr	H (m)
200	3.29	1.00	3.290	60.8	9.73	4.87	20	1	1.00	1.54
100	1.65	1.00	1.645	60.8	9.73	4.87	20.00	1.00	1.00	1.54
50	0.82	1.00	0.823	60.8	9.73	4.87	20.00	1.00	1.00	1.54
21	0.35	0.98	0.354	59.4	9.51	5.38	19.52	0.95	1.00	1.46
10	0.16	0.84	0.195	51.2	8.20	6.93	16.73	0.84	0.99	1.28

d	d/Lo	th(2πd/L)	d/L	L	C	Cg	α	Ks	Kr	H (m)
5	0.08	0.66	0.125	39.9	6.39	8.18	12.98	0.77	0.98	1.17
2	**0.03**	**0.439**	**0.075**	**26.7**	**4.27**	**9.08**	**-8.63**	**0.73**	**0.97**	**1.10**

Tabla 4.9. Propagación del oleaje para ENE (-2.5°N)

d	d/Lo	th(2πd/L)	d/L	L	C	Cg	α	Ks	Kr	H (m)
200	3.24	1.00	3.238	61.8	9.81	4.91	-2.5	1	1.00	1.57
100	1.62	1.00	1.619	61.8	9.81	4.91	-2.50	1.00	1.00	1.57
50	0.81	1.00	0.809	61.8	9.81	4.91	-2.50	1.00	1.00	1.57
21	0.34	0.98	0.349	60.2	9.57	5.44	-2.44	0.95	1.00	1.49
10	0.16	0.84	0.193	51.8	8.22	7.02	-2.09	0.84	1.00	1.31
5	0.08	0.65	0.124	40.3	6.40	8.27	-1.63	0.77	1.00	1.21
2	**0.03**	**0.174**	**0.028**	**35.8**	**1.70**	**9.71**	**-0.43**	**0.71**	**1.00**	**1.12**

Tabla 4.10. Propagación del oleaje para SE (-70°N)

d	d/Lo	th(2πd/L)	d/L	L	C	Cg	α	Ks	Kr	H (m)
200	4.71	1.000	4.701	43	8.14	4.07	-70.00	1.00	1.00	0.73
100	2.35	1.000	2.351	43	8.14	4.07	-70.00	1.00	1.00	0.73
50	1.18	1.000	1.175	43	8.14	4.07	-70.00	1.00	1.00	0.73
21	0.49	0.996	0.496	42	8.11	4.17	-69.39	0.99	0.99	0.71
10	0.24	0.922	0.255	39.2	7.51	5.13	-60.04	0.89	0.83	0.54
5	0.12	0.753	0.156	32.0	6.13	6.36	-45.06	0.80	0.70	0.41
2	**0.05**	**0.517**	**0.091**	**22.0**	**4.21**	**7.37**	**-29.04**	**0.74**	**0.63**	**0.34**

Por último, una vez nuestro frente de oleaje se ha propagado hasta las proximidades del puerto, aplicando los diferentes coeficientes de propagación, al encontrarnos un obstáculo, como es el caso del dique, la ola se ve afectado por el fenómeno de la **difracción**. Este fenómeno provoca que la energía de la ola se transmita de forma lateral a lo largo de la cresta de cada una de ellas al encontrarse con un obstáculo. Además, la altura de ola es variable a lo largo del frente difractado.

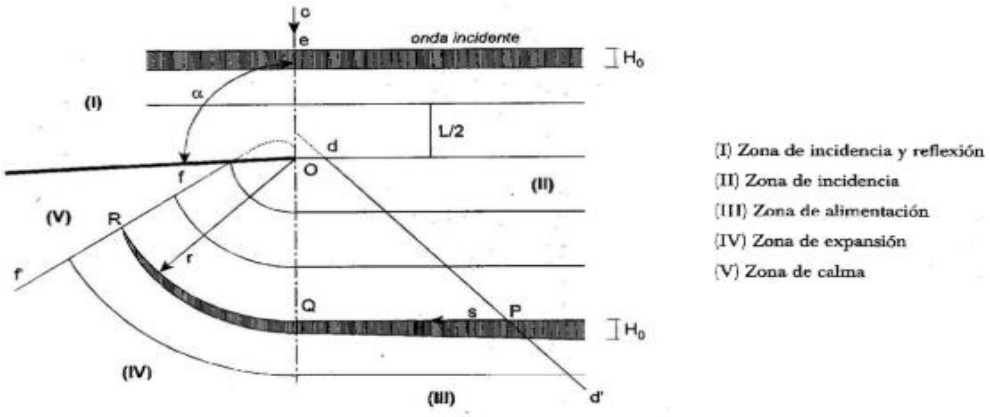

Ilustración 4.8. Fenómeno de difracción

Para el cálculo de la altura de ola una vez la ola ha sido difractada se emplea el *coeficiente de difracción (K_D):*

$$H_{s,d} = H_{s,i} \cdot K_D$$

Donde:

- $H_{s,d}$ es la altura de ola difractada
- $H_{s,i}$ es la altura de ola en el extremo del dique

Para obtener el coeficiente de difracción utilizaremos los ábacos de Wiegel.

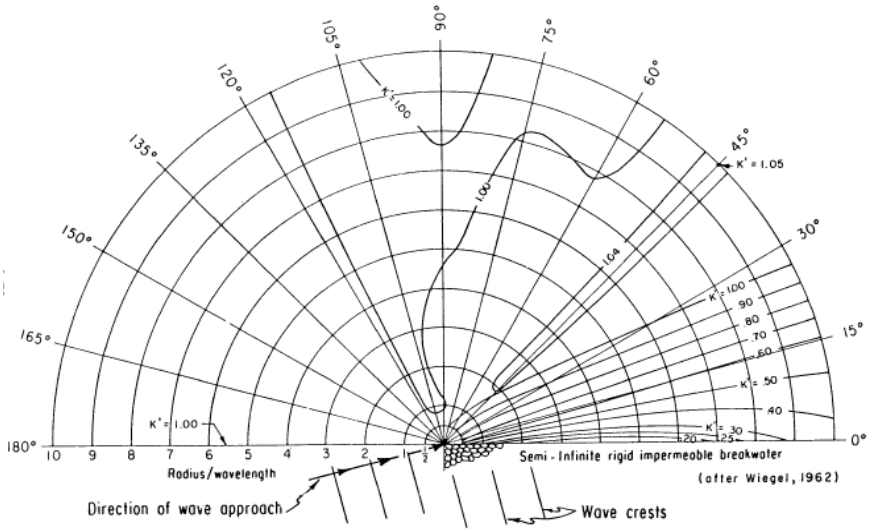

Figure 2-28. Wave diffraction diagram--15° wave angle.

Ilustración 4.9. Ábaco de Wiegel

Como nuestro oleaje direccional predominante proviene del ENE que forma un ángulo prácticamente perpendicular respecto a la alineación de nuestro dique, para un punto en el interior del puerto, ubicado a 40 metros del morro del dique, con un ángulo de respecto al dique de 50° y con un coeficiente entre el radio y la longitud de onda de:

$$\frac{R}{L} = \frac{40}{26.7} = 1.50$$

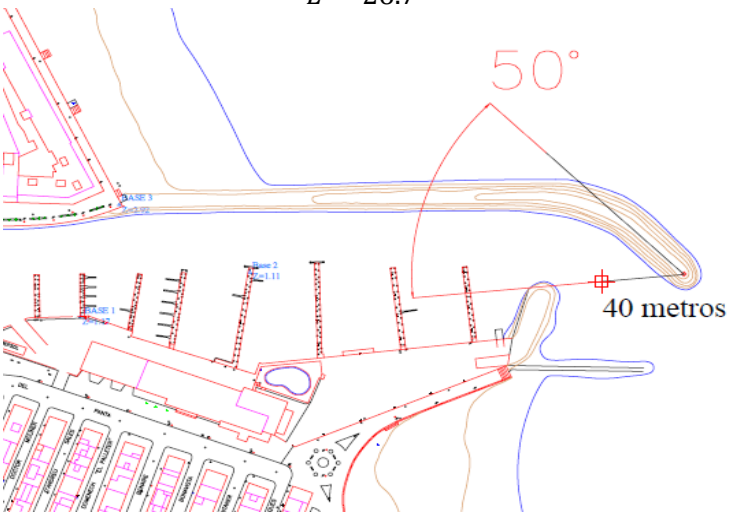

Ilustración 4.10. Punto interno de la dársena para la propagación del oleaje interno

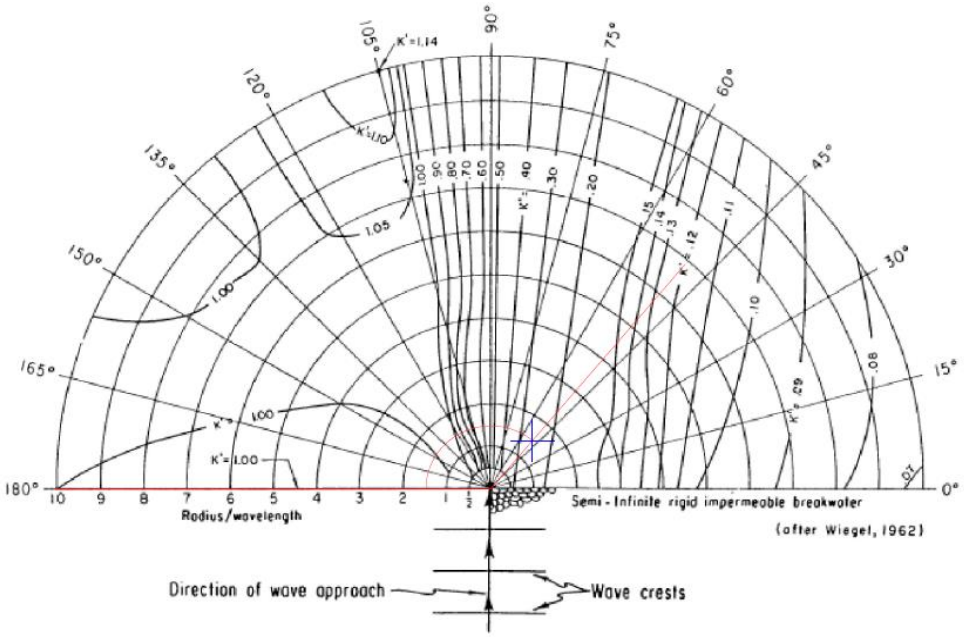

Ilustración 4.11. Ábaco de Wiegel para oleaje en dirección ENE

Por lo tanto, nuestro coeficiente de difracción es, aproximadamente, de 0,28 y nuestra altura de ola a los 40 metros del morro del dique es de:

$$H_{s,d} = 1{,}10 \cdot 0{,}28 = 0{,}308\, m$$

Por otro lado, para la dirección SE, para un punto ubicado a 95 metro en el interior del puerto y un ángulo de 35° respecto a la alineación del dique se tiene el siguiente cociente:

$$\frac{R}{L} = \frac{95}{22} = 4.32$$

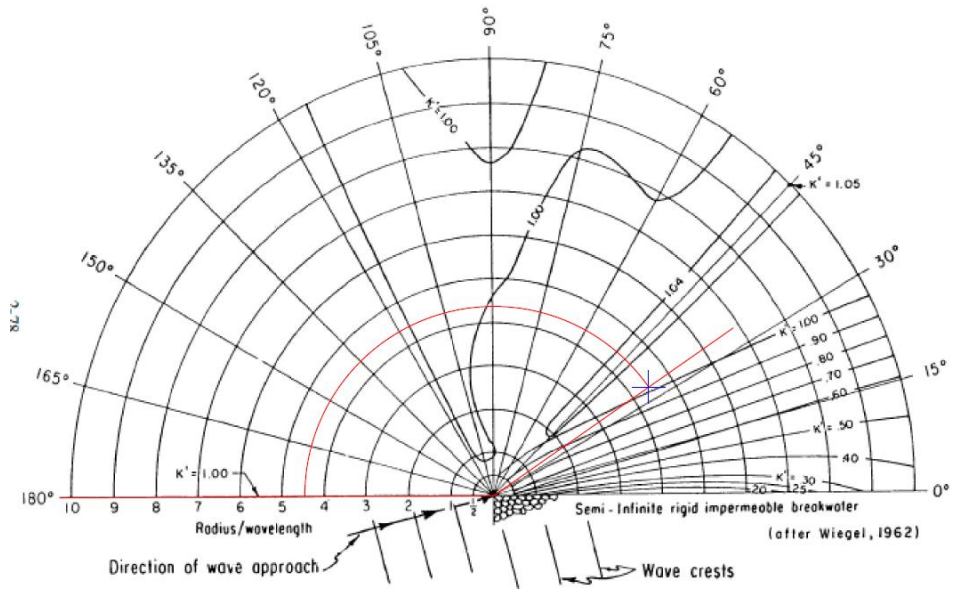

Ilustración 4.12. Ábaco de Wiegel para el oleaje en la dirección SE.

Por lo tanto, nuestro coeficiente de difracción es, aproximadamente, de 1 y nuestra altura de ola a los 95 metros del morro del dique es de:

$$H_{s,d} = 0{,}34 \cdot 1 = 0{,}34\ m$$

3 CARACTERIZACIÓN DEL ESTADO DEL VIENTO

De forma similar a lo establecido en el apartado anterior, para realizar la caracterización de los diferentes Estados del Viento, se han empleado los datos actualizados del Banco de Datos Oceanográficos de Puertos del Estado del Ente Público Puertos del Estado, concretamente a los registros de la boya de Valencia, código 2630. En él se ha sacado la información referente a los regímenes medios. Para la caracterización del viento en regímenes extremales se ha empleado la *ROM 0.4-95 – Acciones climáticas II: Viento.*

3.1 RÉGIMEN MEDIO

En primer lugar, como ya se ha mencionado, para realizar la caracterización del viento en régimen medio se utilizará los datos que proporciona Puertos del Estado en la Boya de Valencia. Del mismo modo que cuando se analizó el oleaje, en estos datos se refleja las series temporales de un conjunto de estados de viento que son más probables que nos encontremos a lo largo de un año.

Analizando las diferentes probabilidades de ocurrencia para cada dirección, se puede observar que la dirección que presenta una mayor ocurrencia durante un periodo anual es la WSW, tal y como se puede observar en la siguiente rosa de vientos:

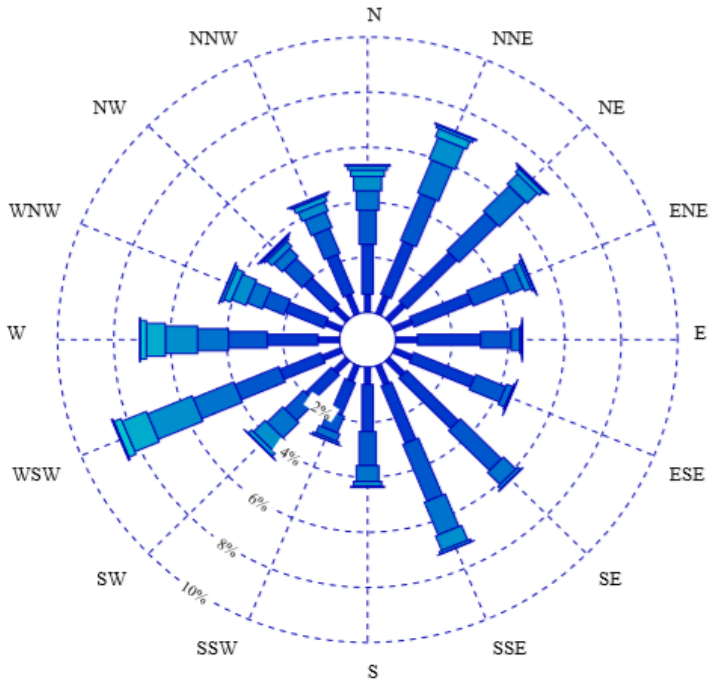

Ilustración 4.43. Rosa de vientos anual

Y, en la siguiente tabla, se muestra el desglose de la distribución conjunta de la dirección y la velocidad media que se puede encontrar en esta zona. En la tabla aparecen remarcadas las direcciones que afectan a nuestra zona de estudio:

Tabla 4.11. Probabilidad de ocurrencia direccional del viento (m/s)

DIRECCIÓN		Ve (m/s)									TOTAL
		≤ 1	2	4	6	8	10	12	14	≥ 14	
CALMAS		12.746									12.746
N	0		0.655	1.808	1.245	0.704	0.517	0.238	0.131	0.066	5.364
NNE	22.5		0.704	2.08	1.835	1.287	0.838	0.307	0.103	0.045	7.199
NE	45		0.783	2.501	1.932	1.294	0.524	0.172	0.059	0.024	7.289
ENE	67.5		0.704	2.232	1.373	0.517	0.241	0.09	0.01	0.017	5.184
ENE	90		0.769	2.242	1.08	0.034	0.069	0.007	0.003	0.003	4.207
ESE	112.5		0.683	2.346	1.156	0.231	0.055	0.003	0.007		4.481
SE	135		0.773	2.704	2.052	0.621	0.124	0.124			6.398
SSE	157.5		0.738	2.253	2.235	1.283	0.576	0.1	0.003		7.188
S	180		0.624	1.711	1.235	0.576	0.179	0.041			4.366
SSW	202.5		0.611	1.273	0.655	0.29	0.093	0.094			3.016
SW	225		0.614	1.294	0.945	0.76	0.583	0.162	0.014	0.007	4.379
WSW	247.5		0.717	1.57	1.683	1.559	1.718	0.935	0.269	0.052	8.503
W	270		0.762	1.801	1.369	1.097	1.142	0.676	0.21	0.031	7.088
WNW	292.5		0.593	1.49	0.8	0.586	0.545	0.255	0.097	0.021	4.387
NW	315		0.635	1.359	0.897	0.41	0.248	0.086	0.052	0.021	3.708
NNW	337.5		0.762	1.514	0.983	0.604	0.348	0.2	0.069	0.017	4.497
TOTAL		**12.746**	**11.127**	**30.178**	**21.475**	**11.853**	**7.8**	**3.49**	**1.027**	**0.304**	**100**

Donde la media ponderada de las velocidades de viento para cada una de las direcciones en un régimen medio es de:

Tabla 4.12. Media ponderada de las velocidades del viento (m/s)

Dirección	Ve (m/s)
SE	5.06
SSE	5.73
S	5.13
SSW	4.85
SW	5.99
WSW	7.44
W	6.87
WNW	6.12
NW	5.38
NNW	5.65

Del mismo modo que se hizo con el oleaje, se realiza un reajuste de la velocidad del viento para cada dirección utilizando la función de distribución Wiebull y que la probabilidad de no excedencia no supere el 0,85, fijado por el *Índice de Repercusión Económica Operativa*:

Tabla 4.13. Ajuste de la velocidad del viento mediante la función de distribución de Weibull

Dirección	SE	SSE	S	SSW	SW	WSW	W	WNW	NW	NNW
F(Ve)	*0.85*	*0.85*	*0.85*	*0.85*	*0.85*	*0.85*	*0.85*	*0.85*	*0.85*	*0.85*
A	*3.72*	*5.32*	*4.23*	*4.03*	*6.67*	*8.99*	*8.32*	*6.71*	*4.65*	*5.78*
B	*0.67*	*0.06*	*0.41*	*0.13*	*-0.88*	*-1.59*	*-1.48*	*-0.75*	*0.25*	*-0.42*
C	*1.98*	*2.3*	*1.95*	*1.97*	*2.5*	*2.93*	*2.65*	*2.11*	*1.58*	*1.88*
Ve	**5.82**	**7.09**	**6.29**	**5.71**	**7.74**	**9.6**	**9.12**	**8.34**	**7.23**	**7.71**

Por otro lado, para la caracterización del régimen extremal utilizamos lo expuesto en el *Atlas de Viento del Litoral Español* de la *ROM 0.4-95 – Acciones climáticas II: Viento.* Nuestra zona de estudio pertenece al Área VII.

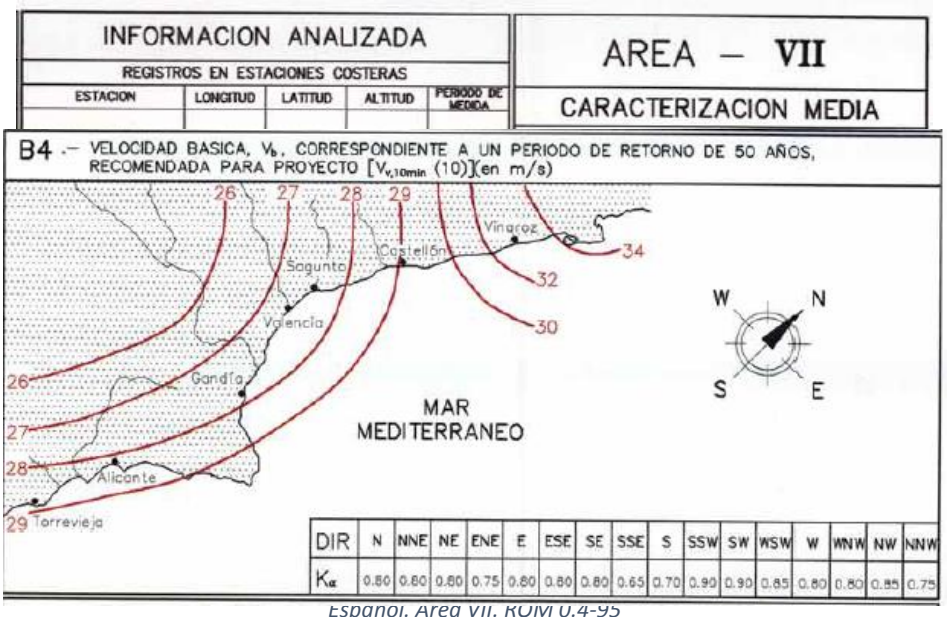

Español. Área VII. ROM 0.4-95

Ilustración 4.104. Velocidad básica de proyecto

La velocidad básica recomendada para el proyecto, correspondiente a un periodo de retorno de 50 años (V_b) es de, aproximadamente, V_b = 27,50 m/s para la zona de estudio, según estable el *Atlas de Viento del Litoral Español*.

Para obtener la velocidad básica direccional asociada al periodo de retorno de la obra se emplea la siguiente ecuación:

$$V_b = V_b(50 a\tilde{n}os) \cdot K_\alpha \cdot K_T$$

Donde:

- K_α: es el coeficiente direccional asociado a cada una de las direcciones a estudiar. En nuestro caso, solo se analizarán las direcciones del viento más desfavorables, que son el WSW.

  Nota: Hay que mencionar que cuando se realizó la *ROM 0.4-95* el viento reinante era el SW, por eso, en la tabla que aparece del en el cuadro B.4 del Área VII del Atlas de Vientos del Litoral Español el coeficiente direccional es de 0,9.

Como se ha podido observar con los datos proporcionados por Puertos del Estado, en la caracterización del viento para un régimen medio, el viento reinante es el WSW para una serie temporal analizada desde septiembre 2005 hasta abril 2017, por lo que, tomaremos para dicha dirección el máximo coeficiente direccional.

- K_T: es el coeficiente de transformación a periodo de retorno de la obra

$$K_T \cong 0{,}75 \cdot \sqrt{1 + 0{,}2 \ln(T)}$$
$$T = 135\ a\tilde{n}os \rightarrow K_T = 1{,}056 \cong 1{,}06$$

Con todos estos datos, la velocidad básica de proyecto para el viento reinante en la zona de estudio es:

$$V_{b,WSW} = 27{,}50 \cdot 0{,}9 \cdot 1{,}06 = 26{,}24\ m/s$$

Además, la velocidad del viento límite en condiciones extremas de operación se ha determinado a partir de la velocidad básica, afectándola los coeficientes que contemplan las condiciones específicas del proyecto:

$$V_{v,t(z)\,T,\alpha} = V_{b\,T,\alpha} \cdot F_A \cdot F_T \cdot F_R$$

Donde:

- $V_{b,T,\alpha}$: Velocidad básica del viento en la dirección asociada a un periodo de retorno T.
- F_A: factor de altura y rugosidad superficial.
  Según la *Tabla 2.1.4.1.1* de la *ROM 0.4-95*, se clasifica la rugosidad superficial en la Categoría I. Como nos encontramos en una zona costera llana, según la *Tabla 2.1.4.1.2.,* para la Categoría I tenemos una F_A = 0,78
- F_T: factor topográfico. La *ROM 0.4-95* considera que los efectos de la topografía local no son significativos para una determinada dirección del viento cuando la pendiente media del terreno a barlovento en una distancia de 5 km desde el punto considerado no exceda de 0,05. En estos casos, se toma F_T = 1
- F_R: factor de ráfaga máxima.
  Para una Categoría I de rugosidad, duraciones de 15 segundos y para una altura de menos de 10 metros, tenemos un factor F_R = 1,41.

Por lo que, tenemos la siguiente velocidad del viento en condiciones extremas:

$$V_{v,15s\,(5),135,WSW} = 26{,}24 \cdot 0{,}78 \cdot 1 \cdot 1{,}41 = 28.86\ m/s$$

4 MAREA

Dada la proximidad al puerto de Valencia, se puede considerar como válidos los datos proporcionados en el Informe del mareógrafo de Valencia (RED de MAReógrafos de Puertos del Estado) para calcular el Nivel del Mar en el puerto de El Perelló.

En la siguiente imagen se puede observar el esquema datum del mareógrafo de Valencia:

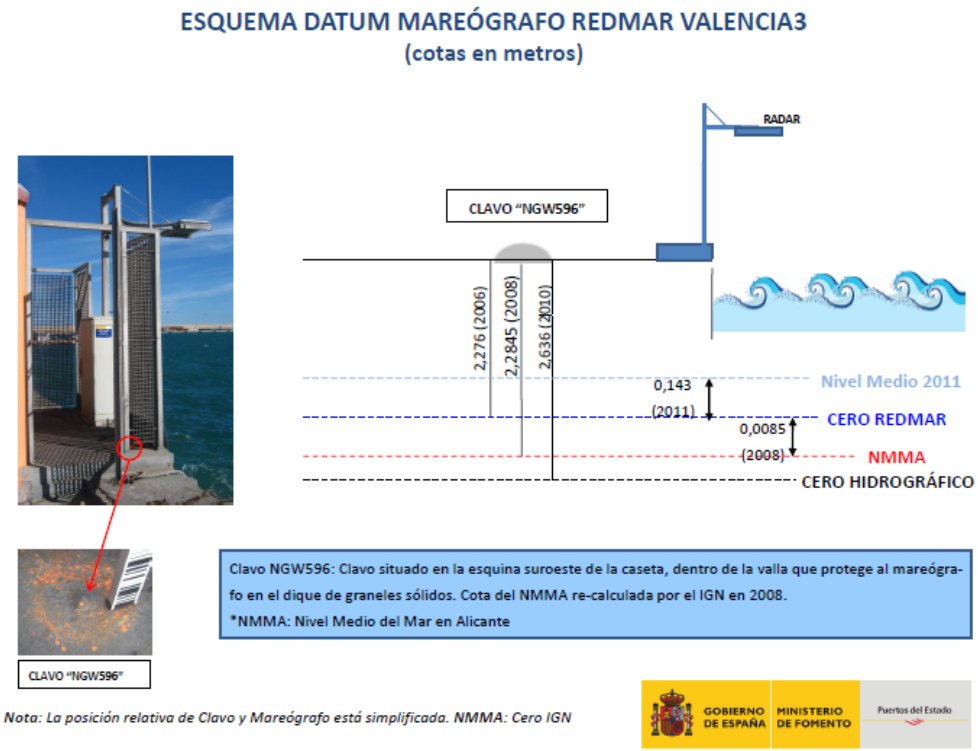

Ilustración 4.115. Esquema datum mareógrafo redmar Valencia. Fuente Puertos del Estado.

En este esquema se reflejan las cotas de los ceros de referencia respecto al clavo de referencia del mareógrafo Valencia3. El NMMA (Nivel Medio del Mar en Alicante) es el origen de altitudes en tierra establecido por el Instituto Geográfico Nacional y que en la península ibérica procede del nivel medio del mar en Alicante durante la década 1870-1880. El *cero hidrográfico*, establecido por el Instituto Hidrográfico de la Marina, coincide aproximadamente con el nivel de agua más bajo y varía con las características de la marea a lo largo de la costa. Por último, el cero REDMAR es el cero de las medidas de los mareógrafos y suele coincidir con el cero del puerto, que, normalmente, suele ser la mínima bajamar.

En la siguiente imagen se refleja un esquema de los diferentes niveles de referencia que hay respecto al mareógrafo. Se puede observar que la carrera de marea astronómica es de 38 centímetros. Si añadimos los efectos de las mareas meteorológicas, la carrera de marea máxima que se ha observado en el puerto de Valencia es de 1,32 metros:

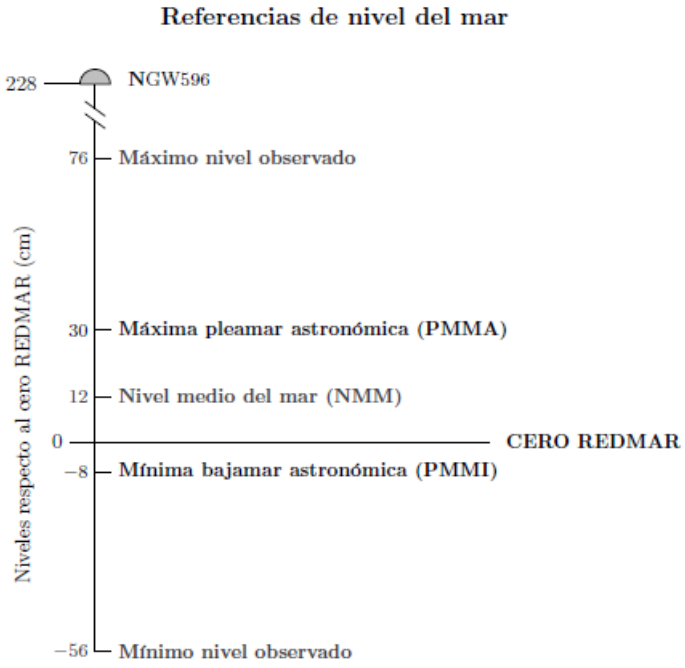

Ilustración 4.16. Referencias de nivel del mar. Mareógrafo Valencia

5 CAMBIO CLIMÁTICO

Debido al incremento de la temperatura global de la Tierra provocado por las emisiones de los gases de efectos invernadero (GEIs), se está generando un deshielo de los casquetes polares a una velocidad considerable, ocasionando un aumento del nivel del mar. Por lo tanto, en cualquier obra civil, y más concretamente en la obra portuaria que vamos a desarrollar, tenemos que tener especial atención a los posibles efectos del aumento del nivel del mar a largo plazo.

Por eso, según se establece en el quinto informe del Grupo Intergubernamental de Expertos sobre el Cambio Climático del 2013 (*Fifth Assessment Report of the Intergovemmental Panel on Climate Change, 2013)*, establecen unas rutas representativas de concentraciones (*Representative Concentration Pathways, RCP)* de GEIs. Estos expertos desarrollaron un total de cuatro escenarios RCP diferentes, Cada uno de ellos representa distintas evoluciones de las concentraciones de GEIs a lo largo del siglo XXI, como son:

- **RCP2.6:** representa un escenario optimista con bajas concentraciones de GEIs.
- **RCP4.**5: representa un escenario moderado con concentraciones de GEIs que se estabilizan antes del 2100.
- **RCP6.0**: representa un escenario moderado con concentraciones de GEIs que se estabilizan después del 2100.
- **RCP8.5:** representa un escenario pesimista con altas concentraciones de GEIs.

En las siguientes gráficas realizadas por el grupo de expertos, se puede observar la predicción de la variación del nivel del mar para los diferentes escenarios hasta el 2100.

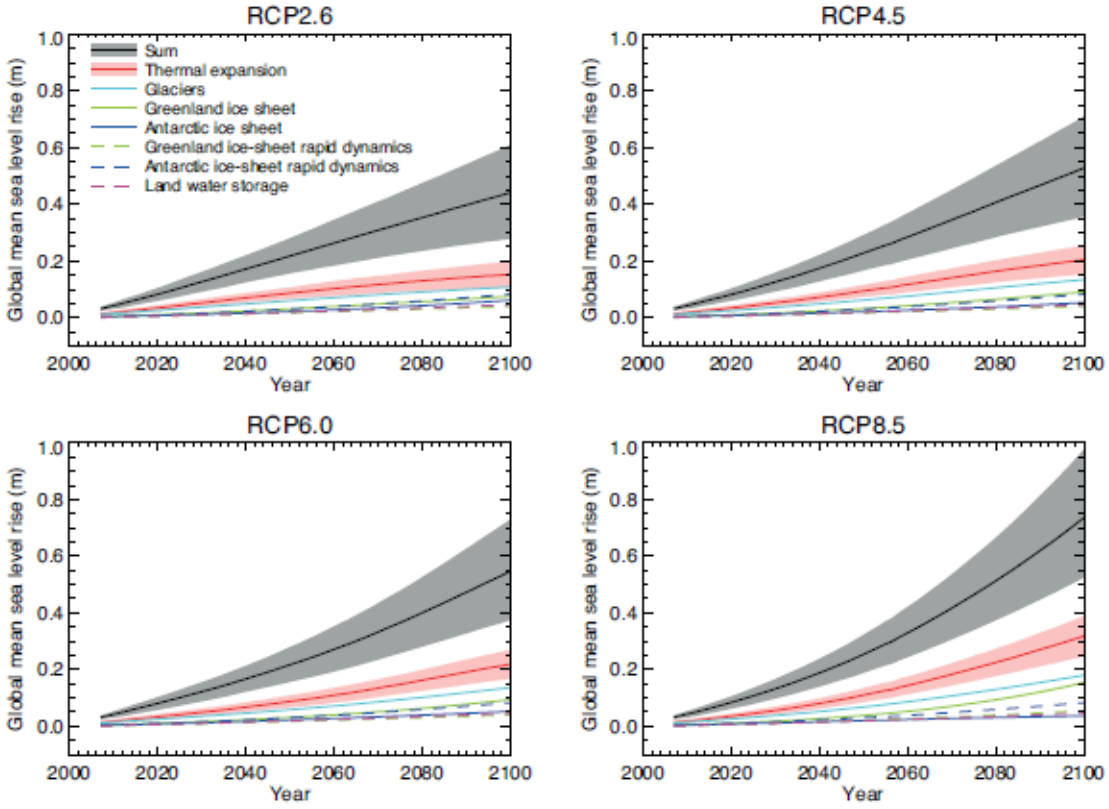

Ilustración 4.147. Gráficas del incremento del nivel del mar. Fuente Quinto Informe del IPCC.

Como se puede observar en el escenario más pesimista, RCP8.5, existe un incremento medio del nivel del mar en el 2100 de 0.74 metros.

Tabla 4.14. Incremento medio del nivel del mar en 2100. Fuente Quinto Informe del IPCC.

	RCP2.6	**RCP4.5**	**RCP6.0**	**RCP8.5**
Incremento global del nivel del mar en 2100 (m)	0,44 (de 0,28 a 0,61)	0,53 (de 0,36 a 0,71)	0,55 (de 0,38 a 0,73)	0,74 (de 0,52 a 0,98)

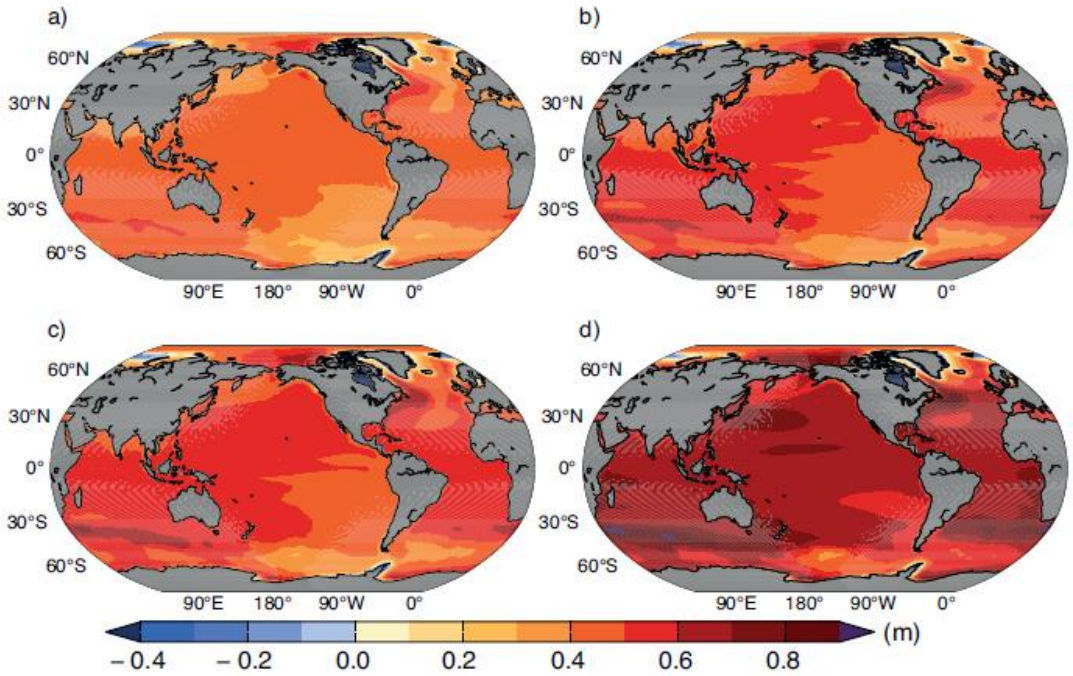

Ilustración 4.158. Mapa del incremento nivel del mar en cada escenario. Fuente Quinto Informe del IPCC

El escenario RCP8.5, al ser un escenario muy pesimista, no se va a tener en cuenta para los futuros cálculos de la coronación de las infraestructuras, por lo tanto, se escogerán los escenarios RCP4.5 y el RCP6.0. La vida útil de nuestro puerto era de 30 años, donde para ambos escenarios rondaríamos los 30 cm de aumento del nivel del mar.

ANEJO I: SEA LEVEL CHANGE

13SM

Sea Level Change
Supplementary Material

Coordinating Lead Authors:
John A. Church (Australia), Peter U. Clark (USA)

Lead Authors:
Anny Cazenave (France), Jonathan M. Gregory (UK), Svetlana Jevrejeva (UK), Anders Levermann (Germany), Mark A. Merrifield (USA), Glenn A. Milne (Canada), R. Steven Nerem (USA), Patrick D. Nunn (Australia), Antony J. Payne (UK), W. Tad Pfeffer (USA), Detlef Stammer (Germany), Alakkat S. Unnikrishnan (India)

Contributing Authors:
David Bahr (USA), Jason E. Box (Denmark/USA), David H. Bromwich (USA), Mark Carson (Germany), William Collins (UK), Xavier Fettweis (Belgium), Piers Forster (UK), Alex Gardner (USA), W. Roland Gehrels (UK), Rianne Giesen (Netherlands), Peter J. Gleckler (USA), Peter Good (UK), Rune Grand Graversen (Sweden), Ralf Greve (Japan), Stephen Griffies (USA), Edward Hanna (UK), Mark Hemer (Australia), Regine Hock (USA), Simon J. Holgate (UK), John Hunter (Australia), Philippe Huybrechts (Belgium), Gregory Johnson (USA), Ian Joughin (USA), Georg Kaser (Austria), Caroline Katsman (Netherlands), Leonard Konikow (USA), Gerhard Krinner (France), Anne Le Brocq (UK), Jan Lenaerts (Netherlands), Stefan Ligtenberg (Netherlands), Christopher M. Little (USA), Ben Marzeion (Austria), Kathleen L. McInnes (Australia), Sebastian H. Mernild (USA), Didier Monselesan (Australia), Ruth Mottram (Denmark), Tavi Murray (UK), Gunnar Myhre (Norway), J.P. Nicholas (USA), Faezeh Nick (Norway), Mahé Perrette (Germany), David Pollard (USA), Valentina Radić (Canada), Jamie Rae (UK), Markku Rummukainen (Sweden), Christian Schoof (Canada), Aimée Slangen (Australia/Netherlands), Jan H. van Angelen (Netherlands), Willem Jan van de Berg (Netherlands), Michiel van den Broeke (Netherlands), Miren Vizcaíno (Netherlands), Yoshihide Wada (Netherlands), Neil J. White (Australia), Ricarda Winkelmann (Germany), Jianjun Yin (USA), Masakazu Yoshimori (Japan), Kirsten Zickfeld (Canada)

Review Editors:
Jean Jouzel (France), Roderik van de Wal (Netherlands), Philip L. Woodworth (UK), Cunde Xiao (China)

This chapter supplementary material should be cited as:
Church, J.A., P.U. Clark, A. Cazenave, J.M. Gregory, S. Jevrejeva, A. Levermann, M.A. Merrifield, G.A. Milne, R.S. Nerem, P.D. Nunn, A.J. Payne, W.T. Pfeffer, D. Stammer and A.S. Unnikrishnan, 2013: Sea Level Change Supplementary Material. In: *Climate Change 2013: The Physical Science Basis. Contribution of Working Group I to the Fifth Assessment Report of the Intergovernmental Panel on Climate Change* [Stocker, T.F., D. Qin, G.-K. Plattner, M. Tignor, S.K. Allen, J. Boschung, A. Nauels, Y. Xia, V. Bex and P.M. Midgley (eds.)]. Available from www.climatechange2013.org and www.ipcc.ch.

Table of Contents

13.SM.1 Methods of Global Mean Sea Level Projections for the 21st Century

This section summarizes the methods used to produce the projections shown in Section 13.5.1 for the Representative Concentration Pathway (RCP) scenarios and the Special Report on Emission Scenarios (SRES) A1B scenario. The Supplementary Material includes files of the annual time series of median, 5th percentile and 95th percentile for each of the contributions to global mean sea level rise and the sum, corresponding to the results shown in Table 13.5. The data files are named as follows:

scenario _ quantity statistic . suffix

for instance *rcp45_summid.nc*. In each name,

scenario is **rcp26**, **rcp45**, **rcp60** or **rcp85**, corresponding to the four representative concentration pathways used in CMIP5, or **sresa1b** for SRES A1B used in CMIP3.

quantity is **temperature** for global mean surface temperature change, **expansion** for thermal expansion (sections 13.4.1 and 13.SM.1.2), **glacier** for glaciers (13.4.2 and 13.SM.1.3), **greensmb** for Greenland ice-sheet SMB (13.4.3.1 and 13.SM.1.4), **antsmb** for Antarctic ice-sheet SMB (13.4.4.1 and 13.SM.1.5), **greendyn** for Greenland ice-sheet rapid dynamical change (13.4.3.2 and 13.SM.1.6), **antdyn** for Antarctic ice-sheet rapid dynamical change (13.4.4.2 and 13.SM.1.6), **landwater** for anthropogenic intervention in water storage on land (13.4.5 and 13.SM.1.6), **greennet** for the sum of SMB and rapid dynamical contributions from the Greenland ice-sheet, **antnet** for the sum of SMB and rapid dynamical contributions from the Antarctic ice-sheet, **sheetdyn** for the sum of the rapid dynamical contributions from the Greenland and Antarctic ice-sheets, or **sum** for the sea level projection including all contributions. Except for temperature, these are the quantities shown in Table 13.5.

statistic is **mid** for the median, or **lower** or **upper** for the limits of the range.

suffix is **txt** for plain ASCII text, or **nc** for netCDF.

The text files have two columns, year and sea level change in metres. The netCDF files describe their contents using the CF convention.

13.SM.1.1 Derivation of Global Surface Temperature and Thermal Expansion Time Series from Coupled Model Intercomparison Project Phase 5

Annual time series for change in global mean surface air temperature (SAT) ('tas' in the CMIP5 archive) and global-mean sea level (GMSL) rise due to thermal expansion ('zostoga') in the historical period and during the 21st century under RCP scenarios (Section 13.4.1) were obtained from a set of 21 CMIP5 AOGCMs (ACCESS1-0, ACCESS1-3, CCSM4, CNRM-CM5, CSIRO-Mk3-6-0, CanESM2, GFDL-CM3, GFDL-ES-M2G, GFDL-ESM2M, HadGEM2-ES, IPSL-CM5A-LR, IPSL-CM5A-MR, MIROC-ESM, MIROC-ESM-CHEM, MIROC5, MPI-ESM-LR, MPI-ESM-MR, MRI-CGCM3, NorESM1-M, NorESM1-ME, inmcm4). These were all those for which thermal expansion was available, including from a parallel pre-industrial control experiment, which is required to remove the thermal expansion due to climate drift in deep-ocean temperatures (Gleckler et al., 2012). The drift was removed by subtracting a polynomial fit as a function of time to the control thermal expansion time series. Where CMIP5 results were not available for a particular Atmosphere–Ocean General Circulation Model (AOGCM) and scenario, they were estimated by the method of Good et al. (2011) and Good et al. (2013) using the response of that AOGCM to an instantaneous quadrupling of carbon dioxide (CO_2) concentration. The same method was used to estimate the CMIP5 projections for scenario SRES A1B. The method gives estimates of change in global mean surface air temperature and net radiative flux at the top of the atmosphere. The

Table 13.SM.1 | Median values and *likely* ranges for projections of global-mean sea level rise and its contributions in metres in 2100 relative to 1986–2005 for the four RCP scenarios and SRES A1B. See Section 13.5.1 concerning how the *likely* range is defined. Because some of the uncertainties in modelling the contributions are treated as uncorrelated, the sum of the lower bound of contributions does not equal the lower bound of the sum, and similarly for the upper bound. Because of imprecision from rounding, the sum of the medians of contributions may not exactly equal the median of the sum.

	SRES A1B	RCP2.6	RCP4.5	RCP6.0	RCP8.5
Thermal expansion	0.24 [0.18 to 0.30]	0.15 [0.11 to 0.20]	0.20 [0.15 to 0.25]	0.22 [0.17 to 0.27]	0.32 [0.25 to 0.39]
Glaciers	0.16 [0.09 to 0.23]	0.11 [0.05 to 0.17]	0.13 [0.07 to 0.20]	0.14 [0.07 to 0.20]	0.18 [0.10 to 0.26]
Greenland Ice Sheet SMB[a]	0.07 [0.03 to 0.15]	0.03 [0.01 to 0.08]	0.05 [0.02 to 0.11]	0.05 [0.02 to 0.12]	0.10 [0.04 to 0.22]
Antarctic Ice Sheet SMB[b]	–0.04 [–0.07 to –0.01]	–0.02 [–0.05 to –0.00]	–0.03 [–0.06 to –0.01]	–0.03 [–0.06 to –0.01]	–0.05 [–0.09 to –0.02]
Greenland Ice Sheet Rapid Dynamics	0.04 [0.01 to 0.06]	0.04 [0.01 to 0.06]	0.04 [0.01 to 0.06]	0.04 [0.01 to 0.06]	0.05 [0.02 to 0.09]
Antarctic Ice Sheet Rapid Dynamics	0.08 [–0.02 to 0.19]	0.08 [–0.02 to 0.19]	0.08 [–0.02 to 0.19]	0.08 [–0.02 to 0.19]	0.08 [–0.02 to 0.19]
Land Water Storage	0.05 [–0.01 to 0.11]	0.05 [–0.01 to 0.11]	0.05 [–0.01 to 0.11]	0.05 [–0.01 to 0.11]	0.05 [–0.01 to 0.11]
Sea Level Rise	0.60 [0.42 to 0.80]	0.44 [0.28 to 0.61]	0.53 [0.36 to 0.71]	0.55 [0.38 to 0.73]	0.74 [0.52 to 0.98]
Greenland Ice Sheet	0.11 [0.07 to 0.19]	0.08 [0.04 to 0.12]	0.09 [0.05 to 0.16]	0.09 [0.06 to 0.16]	0.15 [0.09 to 0.28]
Antarctic Ice Sheet	0.05 [–0.06 to 0.15]	0.06 [–0.04 to 0.16]	0.05 [–0.05 to 0.15]	0.05 [–0.05 to 0.15]	0.04 [–0.08 to 0.14]
Ice-Sheet Rapid Dynamics	0.12 [0.03 to 0.22]	0.12 [0.03 to 0.22]	0.12 [0.03 to 0.22]	0.12 [0.03 to 0.22]	0.14 [0.04 to 0.24]

Only the collapse of the marine-based sectors of the Antarctic Ice Sheet could cause GMSL to rise substantially above the *likely* range during the 21st century. This potential additional contribution cannot be precisely quantified but there is *medium confidence* that it would not exceed several tenths of a meter of sea level rise.

Notes:

[a] Including the height-SMB feedback.

[b] Including the interaction between SMB change and outflow.

latter was integrated in time to obtain the estimated change in heat content of the climate system, and converted to thermal expansion using the expansion efficiency of heat appropriate to each AOGCM, as diagnosed from all the available RCPs for that AOGCM. The correlation between heat content change and thermal expansion is very high and the relationship can be accurately treated as linear (Kuhlbrodt and Gregory, 2012).

13.SM.1.2 Interpretation and Combination of Uncertainties

Uncertainties were derived from the CMIP5 ensemble by treating the model spread as a normal distribution, and following Section 12.4.1.2 it was assumed that the 5 to 95% interval of CMIP5 projections for the 21st century for each RCP scenario can be interpreted as a *likely* range (Section 13.5.1). The CMIP5 timeseries of thermal expansion X and global mean surface air temperature T were expressed as anomalies as a function of time t with respect to their time-means for 1986-2005, and the timeseries of ensemble means $X_M(t)$ and $T_M(t)$ and ensemble standard deviations $X_S(t)$ and $T_S(t)$ were calculated. As in the AR4, a Monte Carlo was used to generate distributions of timeseries of X and T in a perfectly correlated way; for each member of the ensemble, a random number r was chosen from a normal distribution, giving $X(t) = X_M(t) + r\,X_S(t)$ and $T(t) = T_M(t) + r\,T_S(t)$, and $T(t)$ was used to estimate land ice contributions to GMSLR, as described in the following sections. As in the AR4, all the uncertainties described by the land ice methods were assumed to be independent of the climate change uncertainty represented by the variation of r and of one another, except where stated, and were combined by Monte Carlo. Because of the use of Monte Carlo, the results for GMSLR have a random uncertainty. For different random samples of the sizes used to compute the results in Table 13.5, the results vary by up to 0.01 m in GMSLR and its contributions, and 0.1 mm yr^{-1} in the rate of GMSLR. The projections are shown for 2081-2100 in Table 13.5, and for 2100 in Table 13.SM.1.

13.SM.1.3 Glaciers

Changes in glacier mass in all regions excluding Antarctica from 2006 onwards were projected using a parameterized scheme which was fitted separately to results from each of the global glacier models of Giesen and Oerlemans (2013), Marzeion et al. (2012), Radić et al. (2014) and Slangen and van de Wal (2011). For the model of Giesen and Oerlemans (2013), only the dependence on temperature was considered; the dependences on precipitation and atmospheric transmissivity were not included. All of these global glacier models have been used to make projections using output from several AOGCMs. Giesen and Oerlemans used results from CMIP3 AOGCMs for scenario SRES A1B, and the other authors used results from different sets of CMIP5 AOGCMs for RCPs. The RCP results of Slangen and van de Wal (2011) are not included in their published paper, but use the same glacier model as in the paper. The parameterized scheme enables estimates to be made for the glacier contribution to GMSL rise g_I as a function of time t for the consistent set of CMIP3 and CMIP5 AOGCMs across all RCPs and SRES A1B. The scheme gives $g_I(t)$ in millimetres with respect to 2006 as $fI(t)^p$, where $I(t)$ is the time integral of T from 2006 to time t in degrees Celsius year, and the constants f and p used for each glacier model are shown in Table 13.SM.2. The constants were fitted by linear regression of $\log(g)$ against $\log(I)$. The global glacier models on which this formula is based calculate their results from geographically dependent climate change with detailed treatments of glacier surface mass balance (SMB) and the evolution of hypsometry; their complexity cannot be accurately reproduced by a simple formula, and the spread of their results around the prediction of this formula has a coefficient of variation (standard deviation divided by mean) of 20% or less for decadal means for all glacier models and RCPs, except for the early decades of the 21st century under RCP2.6 for the model of Slangen and van de Wal (2011) for which there are fractional errors of up to 40%, but the absolute error is small. Therefore we take 20% of the projection of the formula made using the CMIP5 ensemble mean $I(t)$ as the standard deviation of a normally distributed methodological uncertainty in the glacier projection for each global glacier model. In order to incorporate this uncertainty into the projections, for each member of the Monte Carlo ensemble of glacier time-series, a normally distributed random number was chosen, independent of time, as a factor by which the time-dependent standard deviation should be multiplied, giving the uncertainty to be added to the glacier time-series. We give the four global glacier models equal weight in the projections. Because the time integration began in 2006, a constant 9.5 mm was added to the projections to account for the glacier contribution from 1996 (the centre of the reference period for projections) to 2005; this is the mean result from the model of Marzeion et al. (2012) using input from CMIP5 AOGCM historical experiments. The formula is not applicable beyond 2100 because it does not represent the tendency of global glacier mass to reach a new steady value when global climate stabilizes, although the global glacier models on which it is based can predict this as a consequence of the evolution of hypsometry. Glaciers on Antarctica were not included in the global glacier projections because they are included in the projections for the Antarctic ice sheet.

Table 13.SM.2 | Parameters for the fits to the global glacier models.

Global Glacier Model	f (mm °C^{-1} yr^{-1})	p (no unit)
Giesen and Oerlemans (2013)	3.02	0.733
Marzeion et al. (2012)	4.96	0.685
Radić et al. (2013)	5.45	0.676
Slangen and van de Wal (2011)	3.44	0.742

13.SM.1.4 Greenland Ice Sheet Surface Mass Balance

The change in Greenland ice sheet SMB $G_e(t)$, excluding changes in ice sheet topography, was computed from $T(t)$ using the cubic polynomial formula, Equation (2) of Fettweis et al., which predicts the Greenland SMB anomaly as a function of T, and was obtained by fitting results from an RCM using input from several CMIP5 AOGCMs for RCP4.5 and RCP8.5. Their Equation (2) $G_e = -71.5T - 20.4T^2 - 2.8T^3$ gives G_e in Gt yr^{-1}, which we convert to mm yr^{-1} SLE. In this formula, T is relative to the time mean of 1980–1999, rather than 1986–2005; in the CMIP5 AOGCM results, the former period is cooler by 0.15°C. The results of this formula were compared with those for the same AOGCMs and RCP from Equation (1) of Fettweis et al. (2013), which predicts $G(t)$ from summer (June to August) air temperature at 600 hPa over Greenland. Equation (1) reproduces the RCM results more accurately but cannot be used for the consistent set of CMIP5 AOGCMs and all RCPs because

their required input data are not available. The results of Equation (2) were also compared with those for the same AOGCMs and RCPs with results obtained from the models of Gregory and Huybrechts (2006) and Yoshimori and Abe-Ouchi (2012), the former being the one used in the AR4. As a result of this comparison of projections (Section 13.4.3.1, Table 13.4), $G_e(t)$ was estimated as $FG_2(t)$, where $G_2(t)$ is calculated from T using Fettweis et al. Equation (2), and F is a factor representing methodological uncertainty. This factor is taken to have a log-normal distribution i.e. one of the form $F = e^N$, where N is a normal distribution having a mean of zero. A log-normal distribution is used because the distributions of $G_e(t)$ from the various Greenland ice sheet SMB models are positively skewed. None of these models simulates the change in SMB caused by the evolution of the ice sheet surface topography, which gives a positive feedback on mass loss (Section 13.4.3.2). To allow for this effect, the Greenland ice sheet SMB change $G(t)$ with respect to 1986–2005 was estimated as $EG_e(t)$, where E is a randomly varying factor with a uniform probability distribution in the range 1.00 to 1.15. The uncertainties of E and F were assumed not be correlated, and independent of time. The ice sheet SMB change $G(t)$ was integrated in time to obtain the change in ice sheet mass, starting in 2006. A constant 1.5 mm was added to the projections to account for the Greenland SMB contribution from 1996 (the centre of the reference period for projections) to 2005; this is half of the central observational estimate of the rate of Greenland ice sheet mass loss during this period (Section 13.3.3.2, using data presented in Figure 4.15).

13.SM.1.5 Antarctic Ice Sheet Surface Mass Balance

The change in Antarctic ice sheet SMB $A(t)$ with respect to 1986–2005 was assumed to be due solely to an increase in accumulation (thus, $A < 0$ in units of sea level equivalent, because accumulation on the ice sheet removes mass from the ocean), which was estimated using the results of Gregory and Huybrechts (2006) from CMIP3 AOGCMs. Accumulation was taken to increase at 5.1 ± 1.5% $°C^{-1}$ of warming in Antarctica relative to 1985–2005, the ratio of warming in Antarctic to T was taken to be 1.1 ± 0.2, and the accumulation for the reference period was taken to be 1923 Gt yr^{-1} (Section 13.3.3.2). Both of these uncertainties (standard deviations) were treated as normally distributed methodological uncertainties in the projections. The resulting spread of projections is very close to the spread of the results from the high-resolution Antarctic SMB models of Krinner et al. (2007), Bengtsson et al. (2011) and Ligtenberg et al. (2013) assessed in Section 13.4.4.1. The effect of increased accumulation on the dynamics of the Antarctic ice sheet (Section 13.4.4.2) was taken into account by adding a rate $-SA(t)$ (a positive number in units of sea level equivalent, because the increase in outflow opposes the increase in accumulation and adds mass to the ocean) to the GMSL projections, where S is a randomly varying factor with a uniform probability distribution in the range 0.00 to 0.35. The uncertainties in accumulation sensitivity, Antarctic warming ratio, and the factor S were assumed not to be correlated, but S was perfectly correlated with the distribution of Antarctic rapid ice sheet dynamics (next paragraph), in the sense that when the rapid dynamical increase in outflow is large, the increase in outflow due to the dynamical reaction to increased accumulation is also large. The mass balance changes A and $-SA$ were integrated in time to obtain the change in the ice sheet mass, starting from 2006. Unlike for Greenland ice sheet SMB, no addition to the projections was made to account for the period 1996–2005 for the contribution from Antarctic ice-sheet SMB, because changes during this period are judged to be due solely to dynamical change (Section 13.3.3.2).

13.SM.1.6 Rapid Ice Sheet Dynamics and Anthropogenic Change in Land Water Storage

Following Section 13.3.3.2, the contributions from rapid ice-sheet dynamics at the start of the projections were taken to be half of the observed rate of loss for 2005-2010 from Greenland (half of 0.46-0.80 mm yr^{-1} from Table 4.6) and all of that from Antarctica (0.21-0.61 mm yr^{-1} from Table 4.6). The contributions reach 0.020 to 0.085 m at 2100 from Greenland for RCP8.5, 0.014 to 0.063 m for the other RCPs and –0.020 to 0.185 m from Antarctica for all RCPs; these are the likely ranges from our assessment of existing studies (Sections 13.4.3.2 and 13.4.4.2). For each ice sheet, a quadratic function of time was fitted which begins at the minimal initial rate and reaches the minimum final amount, and another for the maxima. Time series for the rapid dynamic contribution lying between these extremes were constructed as combinations of the extreme time series assuming a uniform probability density between the extremes. Finally, a constant 1.5 mm was added to the contribution from the Greenland ice sheet, and 2.5 mm to the contribution from the Antarctic ice sheet, these being the estimates of those contributions from 1996 to 2005 (using the data presented in Figures 4.15 and 4.16).

The same method was followed for the anthropogenic land water storage contribution (initial rates as for 1993–2010 from Table 13.1 and amounts for the time-mean of 2081-2100 from Section 13.4.5, with no additional amount for land water storage from 1996 to 2005). These contributions are treated as uncorrelated with the magnitude of global climate change and as independent of scenario (except for the higher rate of change for Greenland ice sheet outflow under RCP8.5). This treatment does not imply that the contributions concerned will not depend on the scenario followed, only that the current state of knowledge does not permit a quantitative assessment of the dependence.

13.SM.2 Computation of Regional Maps of Sea Level Change from Coupled Model Intercomparison Project Phase 5 Model Output

Several results and figures in Section 13.6 are based on published methods as referred to in the main text but have not been published independently. This document details all information that led to numbers and figures shown in Section 13.6 on regional sea level projections. Data files for each figure are available.

For each figure or each step involved, the underlying technical details that were used are described. The Supplementary Material includes files containing the data in each case.

Figures 13.15, 13.16 and 13.24 show maps of regional sea level changes computed from CMIP5 coupled climate models. The following steps were pursued in the preparation of those figures.

13.SM.2.1 Sea Surface Height from Coupled Climate Models

Sea surface height (SSH) data, labeled the 'zos' variable, from the CMIP5 AOGCM database, are used to show regional changes in SSH over time, and include the regional variability of dynamic topography changes due to water mass advection, thermohaline circulation and to the wind-driven circulation (see Table 13.SM.3). These regional changes are corrected for regional control drift by removing the linearly fitted control run drift from each latitude–longitude grid box individually, on a per-model basis. After this correction, the global average of this regional SSH field (a function of x, y, t) is forced to be the global thermal expansion ('zostoga' variable) at each time step by first subtracting the globally averaged regional SSH field at each time step from each grid box, and then adding the global thermal expansion time series to each grid box (the same number at every grid box, for a given time). The global thermal expansion time series was also corrected for control drift by removing a quadratic fit to the control run's thermal expansion time series before being added to the regional SSH data. As not all models had multiple ensemble forced runs for the various RCP scenarios, only one run from each model (in each RCP scenario) was used to compute the multi-model ensemble means (i.e., the results for each individual model are only a single realization per scenario, as shown in Figure 13.24).

13.SM.2.2 Interpolation

All of the steps outlined above were performed on each model's own grid, with interpolation to a common 1° × 1° grid only being applied after statistical analyses, to each model's relative sea level changes, means and variances. The interpolation procedure involves applying a nearest-neighbour interpolation and a bilinear interpolation, with the nearest-neighbour interpolation chosen close to the coasts where the bilinear interpolation loses grid boxes.

13.SM.2.3 Masking

Some of the models, on their original grids, had detached marginal seas (e.g., the Mediterranean, Hudson Bay, Baltic Sea, etc.), and in most cases, the SSH in the marginal seas behaved differently than in the nearby ocean, with some models having significant numerical instability, and others undergoing a different SSH evolution in these seas. To remove large and obvious errors from the ensemble mean (and other ensemble statistics) and to treat all the models consistently, marginal seas were masked out from individual models, if they were detached from the adjacent ocean basin, on the common 1° × 1° grid. This results in a final ensemble mean product that consists of, for example, for the RCP4.5 run, a 21-model mean over most of the ocean, but has only as few as 12 ensemble members contributing to the mean for some marginal seas (9 is the lowest number of RCP4.5/8.5 members for which regional data are shown for ensemble statistics).

13.SM.2.4 Combining All Sea Level Rise Components

Figures 13.18, 13.19, 13.22 and 13.23 show projected sea level changes as they result after combining various different contributions to sea level change in addition to those available from CMIP5 models. The following steps were necessary to obtain those maps and figures.

Contributions to regional sea level change due to changes in other components of the climate system were added to the thermosteric/dynamic SSH from the AOGCMs. These components include surface mass balance and dynamic ice sheet contributions from Greenland and Antarctica, a glacier contribution, a land water storage contribution, glacial isostatic adjustment (GIA), and the inverse barometer effect (IBE). The projections of the various land ice contributions and the land water storage contribution are described elsewhere (Sections 13.4, 13.5.1 and 13.SM.1 in the Supplementary Material). These global estimates were turned into regional maps of sea level response, due to the addition of mass increasing the global ocean volume (the barystatic contribution) plus the resultant gravitational and rotational changes, through application of an iterative sea level equation solver (Slangen et al., 2012). The groundwater storage change contribution to regional sea level rise was also found similarly by taking estimates of its geographical distribution from Wada et al. (2012) and applying the same sea level equation solver. The GIA contribution was calculated from the mean of the ICE-5G model (Peltier 2004) and the ANU ice sheet model (Lambeck et al. 1998 and subsequent improvements) with the SELEN code for the sea level equation (Farrell and Clark 1976; Spada and Stocchi 2006, 2007), including updates to allow for coastline variation through time, near-field meltwater damping and Earth rotation in a self-consistent manner (Milne and Mitrovica, 1998; Kendall et al., 2006). The IBE contribution was found by using an ensemble of atmospheric results from the atmospheric component of the same CMIP5 models used for the SSH data. All of these components were calculated 'offline' (i.e., were not part of diagnostic 'zos' and 'zostoga' variables in the models) and then added to the regional sea level rise results previously derived from CMIP5 'zos' and 'zostoga' variables.

13.SM.2.5 Uncertainties

Figures 13.19, 13.21 and 13.23 show uncertainty measures for sea level projections. Those uncertainties were computed as follows.

The uncertainties in the results directly from the CMIP5 model data are estimated with the ensemble spread: one standard deviation of the members' means is treated as the standard error for the ensemble mean. This applies to the dynamic/thermosteric SSH ocean data, and the IBE atmospheric data. The ice sheet, glacier and land water storage uncertainties are found regionally from the global uncertainties of the sources using the same iterative sea level equation solver used to obtain the regional distribution from their means. The one standard error of the GIA uncertainty is evaluated as the departures of the two different GIA estimates (from ICE-5G and ANU/SELEN models) from their mean value. To combine these uncertainties, for both maps of uncertainty as well as time series of uncertainty at individual stations, it is assumed that contributions that correlate with global air temperature have correlated uncertainties, which are therefore added linearly. This combined uncertainty is then added to the other

components' uncertainties in quadrature. The uncertainties in the projected ice sheet SMB changes were assumed to be dominated by the magnitude of climate change, rather than their methodological uncertainty, while the uncertainty in the projected glacier change was assumed to be dominated by its methodological uncertainty. The formula shown below for the regional error, when applied to the global contributions, estimates a global uncertainty close to that given in Table 13.5. The estimated squared uncertainty (standard error) at each grid box is found as follows:

$$\sigma^2_{tot} = (\sigma_{steric/dyn} + \sigma_{smb\_a} + \sigma_{smb\_g})^2 + \sigma^2_{glac} + \sigma^2_{IBE} + \sigma^2_{GIA} + \sigma^2_{LW} + \sigma^2_{dyn\_a} + \sigma^2_{dyn\_g} \quad (13.SM.1)$$

where:

steric/dyn = global thermal expansion uncertainty + dynamic SSH (ensemble spread)

smb_a = Antarctic ice sheet SMB uncertainty (including interaction of SMB and dynamics)

smb_g = Greenland ice sheet SMB uncertainty (including interaction of SMB and dynamics)

glac = Glacier uncertainty

IBE = inverse barometer effect uncertainty (ensemble spread)

GIA = glacial isostatic adjustment uncertainty

LW = land water storage uncertainty

dyn_a = Antarctica ice sheet rapid dynamics uncertainty

dyn_g = Greenland ice sheet rapid dynamics uncertainty

The 90% confidence limits for the ice components are asymmetric and were combined with the 90% confidence limit uncertainties of the CMIP5 ocean components to find the lower and upper uncertainty limits separately (Figures 13.19 and 13.23), using the given equation. In Figure 13.21, in which a single standard error at each location is used, the σ used in the equation were standard deviations for all components except *LW*, *dyn_a* and *dyn_g*; these latter had uniform PDFs in the global projections, and the half-range of the distribution was used for σ. To find the 90% confidence limits of the ocean components, regional uncertainties were multiplied by 1.645, thus treating them as methodological, normally distributed uncertainties.

Table 13.SM.3 | Availability of 'zos' variable from CMIP5.

Model	RCP2.6	RCP6.0	RCP4.5 / RCP8.5
ACCESS-1.0			X
BCC-CSM1.1	X	X	X
CanESM2			X
CNRM-CM5			X
CSIRO-MK3.6.0	X	X	X
GFDL-ESM2G	X	X	X
GFDL-ESM2M	X	X	X
GISS-E2-R	X	X	X
HadGEM2-CC			X
HadGEM2-ES	X		X
INM-CM4			X
IPSL-CM5A-LR	X	X	X
IPSL-CM5A-MR	X		X
MIROC5	X	X	X
MIROC-ESM	X	X	X
MIROC-ESM-CHEM	X	X	X
MPI-ESM-LR	X		X
MPI-ESM-MR	X		X
MRI-CGCM3	X	X	X
NorESM1-M	X	X	X
NorESM1-ME	X	X	X

References

Bengtsson, L., S. Koumoutsaris, and K. Hodges, 2011: Large-scale surface mass balance of ice sheets from a comprehensive atmosphere model. *Surv. Geophys.*, **32**, 459–474.

Farrell, W.E., and Clark, J.A., 1976. On postglacial sea-level, *Geophys. J. R. Astr. Soc.*, **46**, 647–667.

Fettweis, X., B. Franco, M. Tedesco, J. H. van Angelen, J. T. M. Lenaerts, M. R. van den Broeke, and H. Gallee, 2013: Estimating Greenland ice sheet surface mass balance contribution to future sea level rise using the regional atmospheric model MAR. *Cryosphere*, **7**, 469–489.

Giesen, R. H., and J. Oerlemans, 2013: Climate-model induced differences in the 21st century global and regional glacier contributions to sea-level rise. *Clim. Dyn*., **41**, 3283–3300.

Gleckler, P. J., et al., 2012: Human-induced global ocean warming on multidecadal timescales. *Nature Clim. Change*, **2**, 524–529.

Good, P., J. M. Gregory, and J. A. Lowe, 2011: A step-response simple climate model to reconstruct and interpret AOGCM projections. *Geophys. Res. Lett.*, **38**, L01703.

Good, P., J. M. Gregory, J. A. Lowe, and T. Andrews, 2013: Abrupt CO_2 experiments as tools for predicting and understanding CMIP5 representative concentration pathway projections. *Clim. Dyn.*, **40**, 1041–1053.

Gregory, J. M., and P. Huybrechts, 2006: Ice-sheet contributions to future sea-level change. *Philos. Trans. R. Soc. London A*, **364**, 1709–1731.

Kendall, R., Latychev, K., Mitrovica, J.X., Davis, J.E., and Tamisiea, M., 2006. Decontaminating tide gauge records for the influence of Glacial Isostatic Adjustment: the potential impact of 3-D Earth structure, *Geophys. Res. Lett.*, **33**, L24318, doi:10.1029/2006GL028448.

Krinner, G., O. Magand, I. Simmonds, C. Genthon, and J. L. Dufresne, 2007: Simulated Antarctic precipitation and surface mass balance at the end of the twentieth and twenty-first centuries. *Clim. Dyn.*, **28**, 215–230.

Kuhlbrodt, T., and J. M. Gregory, 2012: Ocean heat uptake and its consequences for the magnitude of sea level rise and climate change. *Geophys. Res. Lett.*, **39**, L18608.

Lambeck, K., C. Smither, and P. Johnston, 1998: Sea-level change, glacial rebound and mantle viscosity for northern Europe. *Geophys. J. Int.*, **134**, 102–144.

Ligtenberg, S. R. M., W. J. van de Berg, M. R. van den Broeke, J. G. L. Rae, and E. van Meijgaard, 2013: Future surface mass balance of the Antarctic ice sheet and its influence on sea level change, simulated by a regional atmospheric climate model. *Clim. Dyn.*, **41**, 867–884.

Marzeion, B., A. H. Jarosch, and M. Hofer, 2012: Past and future sea-level changes from the surface mass balance of glaciers. *Cryosphere*, **6**, 1295–1322.

Milne, G.A., and Mitrovica, J.X., 1998. Postglacial sea-level change on a rotating Earth, *Geophys. J. Int.*, **133**, 1–19.

Peltier, W. R., 2004: Global glacial isostasy and the surface of the ice-age earth: The ICE-5G (VM2) model and GRACE. *Annu. Rev. Earth Planet. Sci.*, **32**, 111–149.

Radić, V., A. Bliss, A. D. Beedlow, R. Hock, E. Miles, and J. G. Cogley, 2014: Regional and global projections of twenty-first century glacier mass changes in response to climate scenarios from global climate models. *Clim. Dyn.*, **42**, 37–58.

Slangen, A. B. A., and R. S. W. van de Wal, 2011: An assessment of uncertainties in using volume-area modelling for computing the twenty-first century glacier contribution to sea-level change. *Cryosphere*, **5**, 673–686.

Slangen, A. B. A., C. A. Katsman, R. S. W. van de Wal, L. L. A. Vermeersen, and R. E. M. Riva, 2012: Towards regional projections of twenty-first century sea-level change based on IPCC SRES scenarios. *Clim. Dyn.*, **38**, 1191–1209.

Spada, G., and Stocchi, P., 2006. The Sea Level Equation, Theory and Numerical Examples, Aracne, Roma, p. 96, ISBN: 88–548–0384–7.

Spada, G., and Stocchi, P., 2007. SELEN: a Fortran 90 program for solving the 'Sea Level Equation', *Comput. Geosci.*, **33**(4), 538–562, doi:10.1016/j.cageo.2006.08.006.

Wada, Y., L. P. H. van Beek, F. C. S. Weiland, B. F. Chao, Y. H. Wu, and M. F. P. Bierkens, 2012: Past and future contribution of global groundwater depletion to sea-level rise. *Geophys. Res. Lett.*, **39**, L09402.

Yoshimori, M., and A. Abe-Ouchi, 2012: Sources of spread in multi-model projections of the Greenland ice-sheet surface mass balance. *J. Clim.*, **25**, 1157–1175.